ATMOSPHERIC SCIENCE

Interannual changes in atmospheric oxidation over forests determined from space

Joshua D. Shutter[1], Dylan B. Millet[1]*, Kelley C. Wells[1], Vivienne H. Payne[2], Caroline R. Nowlan[3], Gonzalo González Abad[3]

The hydroxyl radical (OH) is the central oxidant in Earth's troposphere, but its temporal variability is poorly understood. We combine 2012–2020 satellite-based isoprene and formaldehyde measurements to identify coherent OH changes over temperate and tropical forests with attribution to emission trends, biotic stressors, and climate. We identify a multiyear OH decrease over the Southeast United States and show that with increasingly hot/dry summers the regional chemistry could become even less oxidizing depending on competing temperature/drought impacts on isoprene. Furthermore, while global mean OH decreases during El Niño, we show that near-field effects over tropical rainforests can alternate between high/low OH anomalies due to opposing fire and biogenic emission impacts. Results provide insights into how atmospheric oxidation will evolve with changing emissions and climate.

INTRODUCTION

The hydroxyl radical (OH) is the principal tropospheric oxidant, controlling the production and loss of numerous chemicals affecting climate and air quality (*1–3*). For instance, OH is the main sink for short-lived climate forcers including methane, carbon monoxide (CO), and volatile organic compounds (VOCs) (*4*); OH-initiated oxidation of these species in the presence of NO_x ($NO_x = NO + NO_2$) produces tropospheric ozone which is itself a climate forcer and air pollutant. Reactions of OH with SO_2, NO_x, and VOCs also drive formation of aerosols, with resulting effects on human health and on Earth's radiation balance (*4*). Understanding the drivers of OH variability is therefore central to predicting future atmospheric composition.

As a reactive, short-lived (~1 s) species with exceedingly low concentrations (<0.1 parts per trillion), direct OH measurements are analytically difficult and remarkably sparse (*5*). Indirect OH proxies have therefore been developed to probe its distribution and space-time variability. Methyl chloroform (CH_3CCl_3) has been used in this capacity for decades (*6–9*), but declining concentrations due to the Montreal Protocol limit its present-day utility. Other long-lived tracer molecules including ^{14}CO (*10–13*) and CH_4 (*14*) have also been used to gain insights into global and hemispheric OH trends; however, such species are not well-suited for identifying the drivers of OH variability or of associated model errors at smaller spatial scales.

Recent work has begun to use satellite-based measurements of more reactive species to constrain OH variability on smaller spatial scales. Over remote oceanic regions, airborne measurements and model output have been used to parameterize OH abundances in terms of other, more readily observable, species (*15, 16*). Machine learning (ML) approaches have been developed, trained on model output, that use satellite-based inputs to diagnose tropospheric OH patterns over tropical oceans (*17, 18*) and urban regions (*19, 20*). Space-borne NO_2 measurements have also been used to infer urban OH based on the downwind plume evolution (*21–24*). While these approaches have provided insights into OH variability, they have been limited to oceanic or urban regions and either rely on prior model assumptions to train an ML algorithm or require specific urban outflow conditions.

Missing from the above methodologies is the ability to directly constrain OH variability over forest ecosystems—a major gap given that forests cover 31% of Earth's land area and play a critical role in governing atmospheric composition and climate (*25*). Isoprene (C_5H_8) is the predominant biogenic hydrocarbon emitted worldwide (mainly by broadleaf trees and shrubs) (*26*) and is quickly oxidized during daytime to form HCHO as a high-yield product. Wells *et al.* (*27*) showed that the isoprene:HCHO column ratio ($\Omega_{ISOP}:\Omega_{HCHO}$) therefore scales tightly with 1/[OH] on a global basis across seasons, locations, and chemical regimes. While the slope magnitude varies regionally, the $\Omega_{ISOP}:\Omega_{HCHO}$ ratio nonetheless provides a direct and purely observational proxy of atmospheric OH variability that is now measurable from space (*27, 28*).

Here, we combine a new 9-year (2012–2020) record of isoprene column measurements from the CrIS (Cross-track Infrared Sounder; Materials and Methods) satellite sensor with colocated HCHO observations from OMPS (Ozone Mapping and Profiler Suite; Materials and Methods) to uncover regionally coherent OH trends and patterns of variability over key forest ecosystems where isoprene emissions are the main driver of Ω_{HCHO} variability (Materials and Methods). We use the GEOS-Chem chemical transport model (Materials and Methods) as an interpretive tool to diagnose the drivers of these OH changes and to test how well the underlying processes are captured by current understanding. Results show how changing emissions, climate variability, and ecosystem stressors modify the atmosphere's oxidation capacity over biogenic source regions.

RESULTS

Regional trends in OH

Figure 1 maps the 2012–2020 $\Omega_{ISOP}:\Omega_{HCHO}$ trend observed from space by CrIS and OMPS. Over most isoprene source regions worldwide, the ratio trends are statistically insignificant ($P > 0.05$): If any long-term OH trends exist in those areas, then they are not yet detectable above interannual variability. However, two regions stand out with spatially coherent, statistically significant ($P < 0.05$) multiyear trends in $\Omega_{ISOP}:\Omega_{HCHO}$ and therefore in OH: the Southeast United

[1]Department of Soil, Water, and Climate, University of Minnesota, St. Paul, MN 55108, USA. [2]Jet Propulsion Laboratory, California Institute of Technology, Pasadena, CA 91011, USA. [3]Center for Astrophysics | Harvard & Smithsonian, Cambridge, MA 02138, USA.
*Corresponding author. Email: dbm@umn.edu
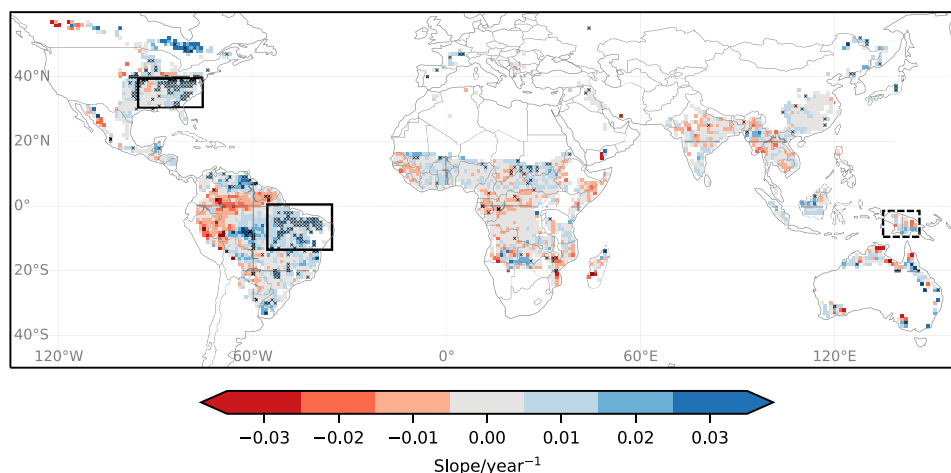
Fig. 1. Annual trends in atmospheric oxidation over isoprene source regions. Plotted are 2012–2020 trends in the isoprene:HCHO column ratio ($\Omega_{ISOP}:\Omega_{HCHO}$) as observed by CrIS and OMPS (see Materials and Methods for details). Red colors indicate negative ratio trends (increasing OH); blue colors indicate positive ratio trends (decreasing OH). Stippling indicates statistical significance at $P < 0.05$. Solid boxes over the Southeast US and East Amazonia indicate analysis domains for spatially coherent, long-term OH trends. The dashed box over New Guinea indicates an analysis domain without any long-term OH trend but with notable interannual variability associated with El Niño.

States (Southeast US) and East Amazonia. We examine the former in detail below. As discussed in Supplementary Text, the OH trend interpretation over East Amazonia is challenged by the larger interannual variability—with the 2012–2020 $\Omega_{ISOP}:\Omega_{HCHO}$ trend statistically significant based on CrIS and OMPS but not when using HCHO data from OMI (Ozone Monitoring Instrument; Materials and Methods).

Figure 2A plots the $\Omega_{ISOP}:\Omega_{HCHO}$ trend observed over the Southeast US (domain in Fig. 1) for 2013–2020. Year 2012 exhibited anomalous behavior due to extreme heat and drought and is examined separately below. We see from Fig. 2A a coherent $\Omega_{ISOP}:\Omega_{HCHO}$ increase that is statistically robust based on both CrIS/OMPS (0.007 ± 0.005 year^{-1}) and CrIS/OMI (0.008 ± 0.005 year^{-1}) observations. Over this time, GEOS-Chem simulations reveal no change in the relationship between $\Omega_{ISOP}:\Omega_{HCHO}$ and 1/OH in terms of either correlation ($r \geq 0.94$) or slope (fig. S2). The trend toward increasing $\Omega_{ISOP}:\Omega_{HCHO}$ ratios seen from the satellite instruments thus points to decreasing OH across the Southeast US.

This trend also manifests in the GEOS-Chem model predictions. Figure 2 (B and C) shows that the base-case model simulation exhibits a consistent $\Omega_{ISOP}:\Omega_{HCHO}$ increase of 0.011 ± 0.004 year^{-1} that is due to a simultaneous decrease in boundary-layer OH of 0.8×10^6 molecules cm^{-3} between 2013 and 2020. This represents a 21% OH decrease during the height of the growing-season (May to September) at the 13:30 local time (LT) satellite overpass time. The statistical agreement between the observed and modeled $\Omega_{ISOP}:\Omega_{HCHO}$ trends corroborates this estimate. The model and satellite data also show a similar degree of interannual variability around the long-term trend (residual SDs of 0.010 and 0.011, respectively). The residuals in both cases have a moderate and positive correlation with temperature [$r = 0.6$ to 0.8 versus surface temperatures from the Modern-Era Retrospective analysis for Research and Applications Version 2 (MERRA-2)], suggesting that variability around the OH trend is caused in part by biogenic VOC emissions or another temperature-dependent process.

Sensitivity analyses indicate that decreasing anthropogenic NO$_x$ emissions drive this OH trend over the Southeast US. US anthropogenic

NO$_x$ emissions declined by an estimated 6 to 7%/year during 2013–2020 (*29–31*), continuing a longer-term pattern (*32, 33*). Figure 2 (B and C) shows that when this NO$_x$ trend is omitted from GEOS-Chem, the temporal $\Omega_{ISOP}:\Omega_{HCHO}$ and OH changes over the Southeast US entirely disappear. Progressively lower NO$_x$ levels reduce the efficiency of both primary (via ozone photolysis) and secondary (via radical recycling) OH generation (*34*), and as a result, we see the Southeast US atmosphere becoming less oxidizing over time.

A notable feature in Fig. 2 (A and B) is that both the satellite-observed and model-predicted $\Omega_{ISOP}:\Omega_{HCHO}$ ratios for 2020 fall slightly below the long-term trend, indicating somewhat elevated OH (this is also seen directly in the model OH fields; Fig. 2C). Prior work has shown on a broader scale that tropospheric OH concentrations were reduced in 2020 due to pandemic-related NO$_x$ reductions (*35*); findings here are specific to the Southeast US during summer and indicate for this area that lower biogenic VOC emissions (~16% lower than 2019 and 2018 based on model predictions; fig. S3) offset the effect of reduced NO$_x$ to yield slightly higher regional OH.

The satellite-observed $\Omega_{ISOP}:\Omega_{HCHO}$ ratios also provide a robust spatial proxy for the atmosphere's oxidation capacity across this domain—with GEOS-Chem simulations showing that the $\Omega_{ISOP}:\Omega_{HCHO}$ distribution closely maps that of 1/[OH] ($r = 0.94$ to 0.98; fig. S2C). Figure 3 shows the observed and predicted $\Omega_{ISOP}:\Omega_{HCHO}$ ratios with the corresponding modeled boundary-layer OH concentrations (13:30 LT) across the Southeast US for July 2013 and 2020. The satellite data reveal a heterogeneous OH distribution across the region, with higher $\Omega_{ISOP}:\Omega_{HCHO}$ ratios (lower OH) over the Ozark forests of southern Missouri and northern Arkansas and lower ratios (higher OH) in more polluted areas surrounding the Mississippi River, southern Illinois, and Indiana. The model captures some of these broad features but strongly overpredicts the observed $\Omega_{ISOP}:\Omega_{HCHO}$ ratios in 2020 over parts of the southern and eastern US (i.e., Georgia, Alabama, and Virginia). More generally, the model tends to overestimate the measured dynamic range: predicting larger differences in $\Omega_{ISOP}:\Omega_{HCHO}$ (and thus in OH) between the low- and high-pollution regions than is observed. Examination of the underlying emission fields suggests that these disparities in part reflect model

uncertainties in the magnitude and variability of isoprene fluxes across this domain. This implies that our models are overestimating the geographic differences in trace gas lifetimes and in the chemical regimes that drive O_3 and aerosol formation across the Southeast US.

We can use the same data to examine the spatial structure of the temporal OH trend identified earlier. Figure 3 (C and F) shows that
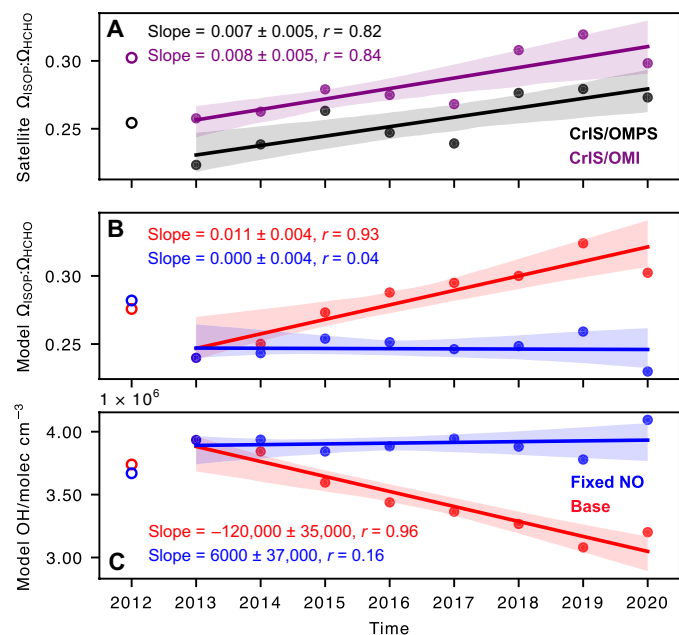
Fig. 2. Multiyear Ω_{ISOP}:Ω_{HCHO} and OH trends over the Southeast US. (**A**) Ω_{ISOP}:Ω_{HCHO} trend observed from space by CrIS/OMPS (black) and CrIS/OMI (purple). (**B**) Modeled Ω_{ISOP}:Ω_{HCHO} trends for the GEOS-Chem base-case simulation (red) and for a sensitivity run where anthropogenic NO emissions are held at 2013 levels (blue). (**C**) OH concentrations simulated by GEOS-Chem at 13:30 local time (LT) using the same color scheme as (B). OH concentrations are averaged vertically through the boundary layer and horizontally across the entire Southeast US domain shown in Fig. 1. Data points represent growing season means computed from monthly spatial averages over the Southeast US for May to September. Lines and shading indicate ordinary least-square fits with 95% confidence intervals. Derived slopes are listed inset in units of $year^{-1}$ (**A** and **B**) or molecules cm^{-3} $year^{-1}$ (**C**). Year 2012 (anomalous heat and drought) is omitted from the regression fits and examined separately below.

the largest observed and predicted Ω_{ISOP}:Ω_{HCHO} change occurs over the Ozarks, implying a major shift in 1/[OH] units. However, the absolute (simulated) [OH] change there is small (Fig. 3I) because concentrations were very low to begin with. Instead, larger absolute OH changes are seen at the periphery of the biogenic source regions where there is greater anthropogenic influence. The model-predicted Ω_{ISOP}:Ω_{HCHO} changes show greater spatial structure than is measured; the observations imply a more spatially diffuse OH trend across the domain.

These results provide an observational demonstration of ongoing OH decreases over the Southeast US, a trend that fits with and helps explain documented regional reductions in O_3 (*36*), organic aerosol (*37–41*), and reactive oxidized nitrogen (*36, 42*). Overall, the chemical climatology of the Southeast US is becoming less oxidizing with a shift to an increasingly NO_x-limited chemical regime. The reduced OH and lower NO_x increase the spatial footprint and change the chemical pathways for VOC oxidation and organic aerosol formation over the Southeast US, with potential implications for both human health and radiative forcing. Longer atmospheric lifetimes may also mean that more biogenically emitted species can survive overnight to initiate morning chemistry and affect air quality in urban areas (*43*).

Ecosystem stress and OH: Intersection of heat and drought over the Ozarks

While the 2013–2020 period shows consistent OH declines across the Southeast US, 2012 stands out over the Ozarks [among the strongest isoprene sources in the world (*27, 44*)] when the region experienced both high temperatures and the most severe seasonal drought since 1895 (*45*). The Ozarks in 2012 thus provide a case study to explore how changing ecosystem stressors such as heat and drought can have chemical feedbacks that change the atmosphere's oxidizing capacity. Such impacts are important to understand given projected increases in both hot extremes and regional drought (*4*).

Figure 4A plots the 2012 CrIS/OMPS Ω_{ISOP}:Ω_{HCHO} ratios for the Ozarks in *z*-score units relative to 2013–2020 (i.e., each month is normalized to the mean and SD for that month in other years). We see strong positive ratio anomalies (abnormally low OH) during May and June, with spatial medians 2.4 and 3.1 SD outside the 2013–2020 monthly norm. The Ozarks then entered a transition period with
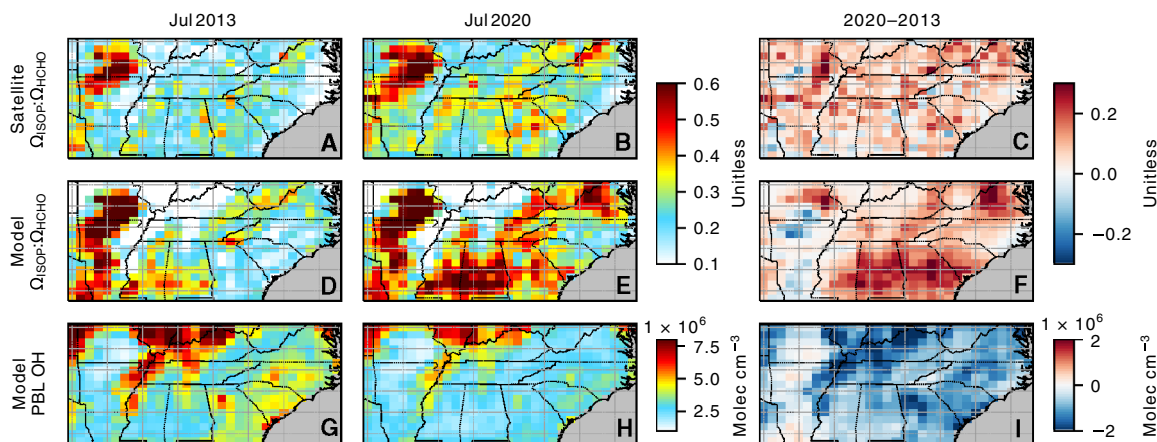
Fig. 3. Spatial distribution of Ω_{ISOP}:Ω_{HCHO} ratios over the Southeast US for July 2013 and 2020 and the 2020–2013 difference. Results are plotted separately for the CrIS/OMPS observations (**A** to **C**) and for the GEOS-Chem model predictions (**D** to **F**). Also mapped are the corresponding OH fields simulated by GEOS-Chem in the planetary boundary layer (PBL) (**G** to **I**).
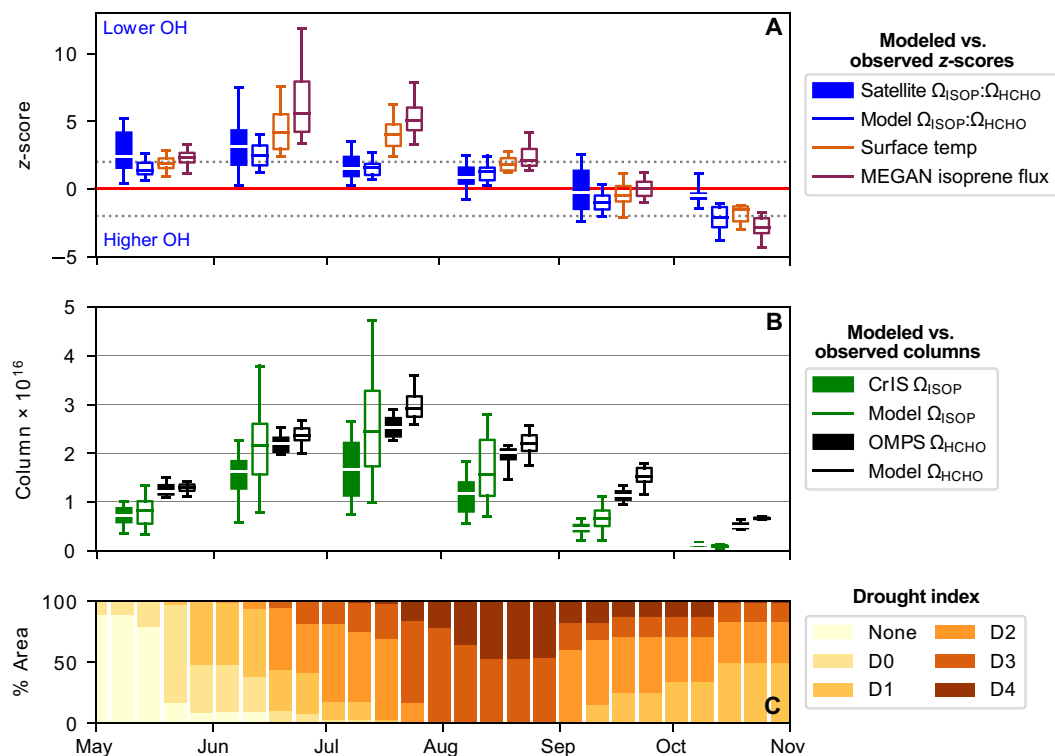
Fig. 4. Effects of extreme heat and drought on atmospheric OH over the Ozarks (35° to 38°N; 90° to 94.375°W) during 2012. (**A**) *Z*-score distributions for the CrIS/OMPS-observed and model-predicted Ω_{ISOP}:Ω_{HCHO} ratios, MERRA-2 surface temperatures, and MEGAN isoprene emissions over the Ozarks from May through October. *Z*-scores are derived on a grid cell basis relative to the monthly means and SDs for outlying years (2013–2020). Dotted lines indicate 2 SDs outside the monthly norm. (**B**) Statistical distributions of isoprene and HCHO columns over the Ozarks as observed from space by CrIS/OMPS and simulated by GEOS-Chem. For both (A) and (B), statistical distributions reflect individual grid cells across the Ozarks domain within a given month; lines and boxes denote the median and interquartile range, while whisker ends indicate the 5th and 95th percentiles. (**C**) Percent of the Ozarks experiencing various categories of drought for the same time period, with none representing no drought and D0 to D4 representing increasing drought severity.

near-average OH during July and August, followed by modestly elevated OH (low Ω_{ISOP}:Ω_{HCHO} ratios) in September and October. These same temporal patterns are likewise seen when using HCHO data from OMI rather than OMPS (fig. S4A), supporting their robustness. The GEOS-Chem model captures these observationally derived OH shifts (and those in the underlying isoprene and HCHO columns; Fig. 4B) but underestimates the magnitude of the early-season OH anomalies.

These OH levels over the Ozarks during 2012 were influenced by a combination of anomalously high heat and exceptional drought. Following the earliest spring onset in the North American record (*46–48*), surface temperatures over the Ozarks during June and July reached their highest values of the CrIS era (Fig. 4). While higher temperatures often increase OH levels due to faster chemistry, elevated ozone, and enhanced soil NO$_x$ emissions (*49*), the initial effect in this case was to suppress OH—as reflected in the high Ω_{ISOP}:Ω_{HCHO} *z*-scores observed through June (Fig. 4A). We attribute this OH suppression to a temperature-driven increase in isoprene emissions, as also predicted by the Model of Emissions of Gases and Aerosols from Nature (MEGAN) implemented within GEOS-Chem (Fig. 4A) and corroborated by ground-based flux observations that were likewise elevated during this first part of the summer (*50*).

By July, there are indications that drought may be affecting OH through suppression of isoprene emissions: While surface temperatures remained anomalously high, the satellite-based Ω_{ISOP}:Ω_{HCHO}

z-scores are substantially reduced from their June values. Figure 4C shows that this timing coincides with extreme to exceptional (D3 and D4) drought conditions over the Ozarks (*51*). Ground-based measurements demonstrate that isoprene emissions in this area were strongly drought suppressed by mid-July 2012 (*50*). The MEGAN-predicted isoprene emissions in Fig. 4A do not account for any such dependence, which, by reducing the modeled isoprene emissions, would increase predicted OH. GEOS-Chem does predict a modest decrease in the Ω_{ISOP}:Ω_{HCHO} *z*-scores from June to July (median: 0.90) but one that is much smaller than the observed change (1.6)—consistent with a missing drought effect. In subsequent months, decreasing surface temperatures and continuing drought conditions combine to further lower isoprene emissions, contributing to more typical or slightly elevated regional OH by September and October.

With its extreme heat and drought, summer 2012 over the Ozarks illustrates how these stressors can have competing effects on OH by either enhancing or suppressing isoprene emissions. Projections from the Intergovernmental Panel on Climate Change Sixth Assessment Report for Central North America indicate a likely to virtually certain increase in the intensity and frequency of hot extremes depending on the degree of warming (1.5° to 4.0°C). For the same amount of warming, there is medium-to-high scientific confidence in increased agricultural/ecological drought for the region (*4*). It is therefore probable that ecosystem stressors like those observed

during summer 2012 will become more frequent and, depending on the competition between heat and drought effects, modulate the NO_x-driven OH trends in this area.

Climate-chemistry interactions: Regional El Niño impacts on OH

The El Niño/Southern Oscillation (ENSO) is a recurring climate feature characterized by anomalously warm sea surface temperatures over the east-central equatorial Pacific Ocean that drives large weather perturbations on regional and global scales. Figure 5A shows, based on the Oceanic Niño Index (ONI), that a very strong (ONI > +2.0) El Niño (i.e., the ENSO warm phase) occurred during the CrIS record in 2015–2016. This event was one of the strongest of the past century, causing historically high temperatures and extreme drought in some regions and extreme rainfall in others (4, 52, 53).

Past studies have shown that global mean OH levels tend to decrease during El Niño events, mainly due to higher fire CO and lower lightning NO_x emissions (54–58). However, the satellite data used here reveal an additional pattern of OH variability due to El Niño that occurs on a regional scale and is distinct from those previously documented global effects. We focus for illustration on the island of New Guinea, which is a global isoprene hotspot residing at the western boundary of the tropical Pacific ENSO domain. Model simulations demonstrate that Ω_{ISOP}:Ω_{HCHO} provides a close proxy for 1/[OH] here (figs. S5 and S6B), and clear El Niño–driven OH variability is seen on this basis. Figure S7B shows that the 2015–2016 El Niño brought the largest positive and the largest negative Ω_{ISOP}:Ω_{HCHO} anomalies seen in this region across the entire 2012–2020 CrIS record.

This observed interannual variability reflects changing boundary-layer oxidation.

The satellite-based Ω_{ISOP}:Ω_{HCHO} ratios in Fig. 5B reveal abnormally elevated OH from August to October 2015 (purple), followed by a 3-month transition, and then a period of abnormally low OH from February to April 2016 (green). The same pattern holds when using HCHO data from OMI rather than OMPS (fig. S6A) and is seen also in the GEOS-Chem model predictions.

These opposing OH effects reflect competing El Niño impacts on isoprene and NO_x. Above-average surface temperatures manifest throughout the El Niño in New Guinea (Fig. 5C), as in much of the tropics. These higher temperatures lead to enhanced isoprene emissions, as seen in Fig. 5C from the MEGAN isoprene flux estimates (which are constrained by leaf area and temperature observations). By themselves, the elevated isoprene emissions would act to suppress OH; however, Fig. 5B shows that this effect only dominates for part of the El Niño (highlighted in green).

Net OH suppression does not occur throughout the El Niño because, along with higher temperatures, 2015 also brought the most severe Indonesian fire season since the early 2000s—which was greatly inflated by the extended El Niño drought (59, 60). Figure 5C shows the boundary-layer NO_2 mixing ratios predicted by GEOS-Chem (which track fire influence since the underlying emissions are constrained by burned-area observations). We see for the purple-shaded months that the elevated fire NO_x overcomes the effect from elevated isoprene emissions and generally causes positive OH anomalies for this part of the El Niño.
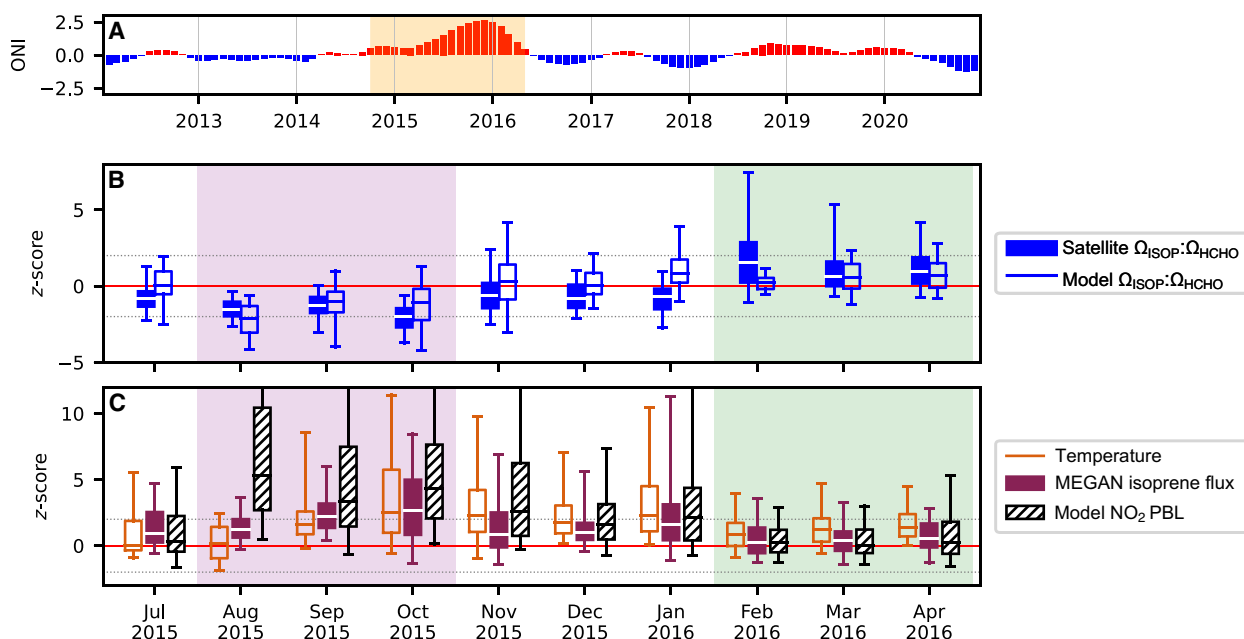
Fig. 5. Variability and drivers of atmospheric oxidation over a tropical forest during El Niño. (**A**) ONI with negative values (blue) indicating La Niña conditions and positive values (red) indicating El Niño conditions. (**B**) Ω_{ISOP}:Ω_{HCHO} z-scores during the strongest part of the 2015–2016 El Niño as observed by CrIS/OMPS or simulated by GEOS-Chem over New Guinea (1.5° to 9.5°S; 135° to 146.25°E). (**C**) Z-scores for MERRA-2 surface temperatures, MEGAN isoprene emissions, and GEOS-Chem–simulated NO_2 mixing ratios (boundary-layer mean) for the same location. Figure S8 shows the full vertical axis in (C). Z-scores are derived on a grid cell basis relative to the monthly means and SDs for non–El Niño conditions [nonshaded regions of (A)]. Dotted lines indicate 2 SDs outside the monthly norm. Statistical distributions in (B) and (C) reflect individual grid cells across the New Guinea domain within a given month; lines and boxes denote the median and interquartile range, while whisker ends indicate the 5th and 95th percentiles. Green shading indicates periods with anomalously high Ω_{ISOP}:Ω_{HCHO} ratios (low OH); purple shading indicates periods with anomalously low Ω_{ISOP}:Ω_{HCHO} ratios (high OH).

Overall, while El Niño events are linked exclusively to OH decreases on a global mean basis (a pattern also seen in the GEOS-Chem simulations used here; fig. S9), the short-lived chemical tracers used in this study show that this global effect encompasses opposing (time-dependent) regional-scale effects. Specifically, for the New Guinean tropical forest examined above, the satellite-based isoprene and HCHO observations reveal alternating positive and negative OH anomalies that depend on the temporal phase and magnitude of offsetting effects from isoprene and fire NO$_x$ emissions—which are both elevated during El Niño.

Extreme climate impacts like those associated with the 2015–2016 El Niño are predicted to occur more frequently with increased global warming (4). Over the Indonesian region, more intense fire episodes are expected during future El Niño droughts in the absence of land-use reforms (60). The 2015–2016 El Niño thus provides insight into how the atmosphere's oxidizing capacity will respond in a warming climate over many tropical forests. Outside of the fire season, we expect suppressed OH due to enhanced isoprene emissions, with the greater quantity of emitted biogenic carbon then oxidized farther afield. During periods of increased biomass burning, along with the fire emissions themselves, faster chemical processing of biogenic emissions will enhance regional formation of oxygenated VOCs, ozone, and secondary organic aerosol—with their associated air quality impacts.

DISCUSSION

We have used space-based observations of the isoprene:HCHO column ratio (Ω_{ISOP}:Ω_{HCHO}) to identify and explain trends and interannual variability in OH over forest ecosystems. Measurements from the CrIS and OMPS sensors onboard the Suomi National Polar–orbiting Partnership (Suomi-NPP) satellite reveal a coherent decreasing trend in OH over the Southeast US that we show is due to declining anthropogenic NO$_x$. Model simulations incorporating this NO$_x$ reduction reproduce the satellite-observed Ω_{ISOP}:Ω_{HCHO} trend and suggest that daytime (13:30 LT) OH levels declined by >20% over the Southeast US during the height of the growing season between 2013 and 2020. This trend is consistent with and helps explain past observations of decreasing regional O$_3$, NO$_x$, SO$_2$, and organic aerosol, reflecting a shifting chemical climatology in the Southeast US. This shift to less oxidizing conditions could be accelerated if extremely hot, dry summers like that of 2012 become more commonplace—depending on the competing effects of heat and drought that respectively enhance and suppress isoprene emissions. On a broader scale, we find from model sensitivity tests that if the 2013–2020 US decrease in anthropogenic NO$_x$ emissions were also to occur globally, the atmospheric methane lifetime would increase by approximately 6%.

We also identified interannual patterns of OH variability for a key tropical rainforest. These El Niño–driven OH anomalies reflect opposing impacts from biogenic isoprene and fire NO$_x$ on atmospheric oxidation, with both of these drivers strongly enhanced during 2015–2016. Past research has shown that El Niño events are associated with reduced global mean OH, but this work using shorter-lived tracers demonstrates that, regionally, OH over tropical forests can alternate between high and low anomalies according to the timing of the fire season. Satellite-based observations of the Ω_{ISOP}:Ω_{HCHO} ratio thus provide insights into how OH may respond over forests in a future with increased likelihood of El Niño–induced extremes.

The combination of space-based isoprene and HCHO observations provides a powerful constraint for understanding oxidative chemistry over isoprene source regions. The Joint Polar Satellite System satellite series is expected to provide a long-term record for both species extending well into the 2030s, providing a critical data record for characterizing OH changes under a shifting climate and biosphere. This Ω_{ISOP}:Ω_{HCHO}-based constraint can further complement existing OH proxies for oceanic and urban areas to create a more globally complete map of spatially resolved OH changes over time.

MATERIALS AND METHODS
Satellite observations
The CrIS and OMPS instruments are both onboard the Suomi-NPP satellite launched in October 2011. Suomi-NPP is in a Sun-synchronous orbit with 13:30 LT daytime Equator overpass, coinciding with peak isoprene emission, photochemistry, and boundary-layer mixing.

CrIS is a Fourier transform spectrometer with a resolution of 0.625 cm^{-1} in the longwave infrared (650 to 1095 cm^{-1}). Daily gridded (0.5° × 0.625°) isoprene columns analyzed here were derived using the Retrieval of Organics from CrIS Radiances (ROCR) algorithm developed by Wells et al. (61), which uses a hyperspectral range index calculated from level 1B CrIS spectra over land and cloud screening based on (27). The ROCR isoprene columns compare well with optimal estimation retrievals and with ground-based Fourier transform infrared isoprene column measurements from Porto Velho in Amazonia (20 to 50% discrepancies reflecting different types of systematic uncertainty) (27, 28, 61).

OMPS measures backscattered ultraviolet (UV) light (300 to 380 nm) with 1-nm spectral resolution. HCHO slant columns used here are as described by Nowlan et al. (62). We apply the recommended reference sector and bias corrections to the level 2 (L2) swath data (see Data and Materials Availability) and convert to vertical columns using modified air mass factors constructed from GEOS-Chem HCHO profiles (see below). Standard data screening is applied (eliminating pixels with solar zenith angle > 70°, cloud fraction > 0.4, snow/ice fraction > 0.02, or main data quality flag > 1) before oversampling the daily L2 swath data to the 0.5° × 0.625° CrIS isoprene resolution (63). Evaluation of the OMPS-NPP HCHO data against ground-based column observations indicates a mean bias of −0.9% across all sites (+20% for Ω_{HCHO} < 4 × 10^{15} molecules cm^{-2}; −15% for Ω_{HCHO} > 4 × 10^{15} molecules cm^{-2}) (64).

OMI is a near-UV/visible spectrometer onboard the Aura satellite launched in 2004 and has a Sun-synchronous orbit with a 13:45 LT daytime Equator overpass. OMI covers a spectral range from 264 to 504 nm with a resolution of 0.42 to 0.63 nm. Monthly gridded (level 3) OMI HCHO (QA4ECV; see Data and Materials Availability) was regridded to the CrIS isoprene resolution. Total vertical column uncertainty ranges from 25 to 50% (65). OMI HCHO data are used here to test and corroborate the Ω_{ISOP}:Ω_{HCHO} patterns from CrIS and OMPS.

Filtering procedure and domain boundaries
Daily satellite observations and the corresponding model values are removed from further analyses in cases of missing isoprene or HCHO data and where water composes 40% or more of the grid cell surface area [based on observations from the Moderate Resolution Imaging Spectroradiometer (MODIS) onboard Terra + Aqua (66)]. We further restrict analyses to locations where isoprene emissions are the main driver of Ω_{HCHO} variability. Past work has used the strong linear relationship between Ω_{HCHO} and isoprene emissions to show where

HCHO variability is dominated by isoprene and to quantify the underlying emissions (*67*, *68*). We adopt an analogous approach to screen locations appreciably affected by non-isoprene HCHO sources. Specifically, we plot the ensemble of daily HCHO columns predicted by GEOS-Chem across each domain against the underlying isoprene emissions from February 2012 to December 2020. Situations with unusually elevated Ω_{HCHO} values for a given isoprene emission arise when there is a major HCHO input from biomass burning. We find that such grid cells can be effectively removed based on a fire HCHO emission threshold of $> 2 \times 10^{-12}$ kg m^{-2} s^{-1} as predicted by the Global Fire Emissions Database Version 4 (GFED4; fig. S1). While this threshold relies on bottom-up emission estimates, those estimates are constrained using satellite observations of burned area.

Monthly mean isoprene and HCHO columns were then computed for each grid cell. Grid cells with low measured column amounts (monthly mean Ω_{ISOP} or $\Omega_{HCHO} < 1 \times 10^{15}$ molecules cm^{-2}) were excluded from both the satellite and model datasets to reduce noise and ensure robust interpretation of the Ω_{ISOP}:Ω_{HCHO} ratios. Long-term trends mapped in Fig. 1 were derived by then averaging the monthly mean ratios by year. Additional filtering depended on the domain. The Southeast US trend analysis (31° to 39°N; 76.25° to 95°W) focuses on the growing season (May to September). The heat and drought analysis over the Ozarks (35° to 38°N; 90° to 94.375°W) extends from May to October with MODIS/Terra + Aqua data used to mask out urban (>5%) and cropland (>15%) grid cells. East Amazonia (0° to 13°S; 35.625° to 55°W) was selected according to the spatial distribution of increasing Ω_{ISOP}:Ω_{HCHO} ratios shown in Fig. 1, with interpretation in Supplementary Text then focusing on the nonfire season (March to July). Last, MODIS/Terra + Aqua data were used to mask out urban (>2%) grid cells for the New Guinea (1.5° to 9.5°S; 135° to 146.25°E) domain.

GEOS-Chem simulations

We use the GEOS-Chem three-dimensional chemical transport model (v.13.3.2; https://doi.org/10.5281/zenodo.5711194) to interpret the space-based observations. After a 1-year model spin-up, global 2° × 2.5° runs were performed for February 2012 to December 2020 using MERRA-2 assimilated meteorological fields on 47 vertical layers with time steps of 600 s (transport/convection) and 1200 s (chemistry/emissions). The model features full HO$_x$-NO$_x$-O$_x$-VOC-Br-Cl-I chemistry coupled to aerosols, incorporating recent updates for isoprene (*69*) and the latest chemical rate recommendations. Online biogenic emissions use MEGAN version 2.1 (*26*), while biomass burning emissions are computed on a diurnally varying basis using GFED4 (v2020-02) (*70–74*). Anthropogenic emissions use CEDS (v2021-06) (*29*, *30*). Since 2020 CEDS data were unavailable at the time of analysis, anthropogenic NO emissions for that year are estimated from the 2019 values with a 2020:2019 scale factor for the US (*31*) applied uniformly across the globe. Anthropogenic emissions for other species in 2020 use their 2019 CEDS values. Soil and lightning NO$_x$ emissions are computed offline (*75–77*). Nested simulations were performed on the native MERRA-2 grid (0.5° × 0.625°) and used for all regional analyses. These nested grid simulations used initial and boundary conditions from the global runs and were configured as above, except using time steps of 300 s (transport/convection) and 600 s (chemistry/emissions). All modeled outputs were time-averaged (12:00 to 15:00 LT) according to the Suomi-NPP overpass time.

Supplementary Materials

This PDF file includes:
Supplementary Text
Figs. S1 to S9
Table S1

REFERENCES AND NOTES

1. H. Levy, Normal atmosphere: Large radical and formaldehyde concentrations predicted. *Science* **173**, 141–143 (1971).
2. J. A. Logan, M. J. Prather, S. C. Wofsy, M. B. McElroy, Tropospheric chemistry: A global perspective. *J. Geophys. Res.* **86**, 7210–7254 (1981).
3. C. M. Spivakovsky, J. A. Logan, S. A. Montzka, Y. J. Balkanski, M. Foreman-Fowler, D. B. A. Jones, L. W. Horowitz, A. C. Fusco, C. A. M. Brenninkmeijer, M. J. Prather, S. C. Wofsy, M. B. McElroy, Three-dimensional climatological distribution of tropospheric OH: Update and evaluation. *J. Geophys. Res.* **105**, 8931–8980 (2000).
4. V. Masson-Delmotte, P. Zhai, A. Pirani, S. L. Connors, C. Péan, S. Berger, N. Caud, Y. Chen, L. Goldfarb, M. I. Gomis, M. Huang, K. Leitzell, E. Lonnoy, J. B. R. Matthews, T. K. Maycock, T. Waterfield, O. Yelekçi, R. Yu, B. Zhou, Eds., *Climate Change 2021: The Physical Science Basis. Contribution of Working Group I to the Sixth Assessment Report of the Intergovernmental Panel on Climate Change* (Cambridge University Press, 2021); https://ipcc.ch/report/ar6/wg1/.
5. D. E. Heard, M. J. Pilling, Measurement of OH and HO$_2$ in the troposphere. *Chem. Rev.* **103**, 5163–5198 (2003).
6. J. E. Lovelock, Methyl chloroform in the troposphere as an indicator of OH radical abundance. *Nature* **267**, 32 (1977).
7. H. B. Singh, Preliminary estimation of average tropospheric HO concentrations in the northern and southern hemispheres. *Geophys. Res. Lett.* **4**, 453–456 (1977).
8. S. A. Montzka, M. Krol, E. Dlugokencky, B. Hall, P. Jöckel, J. Lelieveld, Small interannual variability of global atmospheric hydroxyl. *Science* **331**, 67–69 (2011).
9. P. K. Patra, M. C. Krol, R. G. Prinn, M. Takigawa, J. Mühle, S. A. Montzka, S. Lal, Y. Yamashita, S. Naus, N. Chandra, R. F. Weiss, P. B. Krummel, P. J. Fraser, S. O'Doherty, J. W. Elkins, Methyl chloroform continues to constrain the hydroxyl (OH) variability in the troposphere. *J. Geophys. Res.* Atmos. **126**, e2020JD033862 (2021).
10. B. Weinstock, Carbon monoxide: Residence time in the atmosphere. *Science* **166**, 224–225 (1969).
11. B. Weinstock, H. Niki, Carbon monoxide balance in nature. *Science* **176**, 290–292 (1972).
12. J. E. Mak, J. R. Southon, Assessment of tropical OH seasonality using atmospheric ^{14}CO measurements from Barbados. *Geophys. Res. Lett.* **25**, 2801–2804 (1998).
13. M. R. Manning, D. C. Lowe, R. C. Moss, G. E. Bodeker, W. Allan, Short-term variations in the oxidizing power of the atmosphere. *Nature* **436**, 1001–1004 (2005).
14. Y. Zhang, D. J. Jacob, J. D. Maasakkers, M. P. Sulprizio, J.-X. Sheng, R. Gautam, J. Worden, Monitoring global tropospheric OH concentrations using satellite observations of atmospheric methane. *Atmos. Chem. Phys.* **18**, 15959–15973 (2018).
15. G. M. Wolfe, J. M. Nicely, J. M. St. Clair, T. F. Hanisco, J. Liao, L. D. Oman, W. B. Brune, D. Miller, A. Thames, G. González Abad, T. B. Ryerson, C. R. Thompson, J. Peischl, K. McKain, C. Sweeney, P. O. Wennberg, M. Kim, J. D. Crounse, S. R. Hall, K. Ullmann, G. Diskin, P. Bui, C. Chang, J. Dean-Day, Mapping hydroxyl variability throughout the global remote troposphere via synthesis of airborne and satellite formaldehyde observations. *Proc. Natl. Acad. Sci. U.S.A.* **116**, 11171–11180 (2019).
16. C. B. Baublitz, A. M. Fiore, S. M. Ludwig, J. M. Nicely, G. M. Wolfe, L. T. Murray, R. Commane, M. J. Prather, D. C. Anderson, G. Correa, B. N. Duncan, M. Follette-Cook, D. M. Westervelt, I. Bourgeois, W. H. Brune, T. P. Bui, J. P. DiGangi, G. S. Diskin, S. R. Hall, K. McKain, D. O. Miller, J. Peischl, A. B. Thames, C. R. Thompson, K. Ullmann, S. C. Wofsy, An observation-based, reduced-form model for oxidation in the remote marine troposphere. *Proc. Natl. Acad. Sci. U.S.A.* **120**, e2209735120 (2023).
17. D. C. Anderson, M. B. Follette-Cook, S. A. Strode, J. M. Nicely, J. Liu, P. D. Ivatt, B. N. Duncan, A machine learning methodology for the generation of a parameterization of the hydroxyl radical. *Geosci. Model Dev.* **15**, 6341–6358 (2022).
18. D. C. Anderson, B. N. Duncan, J. M. Nicely, J. Liu, S. A. Strode, M. B. Follette-Cook, Technical note: Constraining the hydroxyl (OH) radical in the tropics with satellite observations of its drivers – first steps toward assessing the feasibility of a global observation strategy. *Atmos. Chem. Phys.* **23**, 6319–6338 (2023).
19. Q. Zhu, J. L. Laughner, R. C. Cohen, Estimate of OH trends over one decade in North American cities. *Proc. Natl. Acad. Sci. U.S.A.* **119**, e2117399119 (2022).
20. Q. Zhu, J. L. Laughner, R. C. Cohen, Combining machine learning and satellite observations to predict spatial and temporal variation of near surface OH in North American cities. *Environ. Sci. Technol.* **56**, 7362–7371 (2022).
21. S. Beirle, K. F. Boersma, U. Platt, M. G. Lawrence, T. Wagner, Megacity emissions and lifetimes of nitrogen oxides probed from space. *Science* **333**, 1737–1739 (2011).
22. L. C. Valin, A. R. Russell, R. C. Hudman, R. C. Cohen, Effects of model resolution on the interpretation of satellite NO$_2$ observations. *Atmos. Chem. Phys.* **11**, 11647–11655 (2011).

23. L. C. Valin, A. R. Russell, R. C. Cohen, Variations of OH radical in an urban plume inferred from NO_2 column measurements. *Geophys. Res. Lett.* **40**, 1856–1860 (2013).

24. S. Lama, S. Houweling, K. F. Boersma, I. Aben, H. A. C. Denier van der Gon, M. C. Krol, Estimation of OH in urban plumes using TROPOMI-inferred NO_2/CO. *Atmos. Chem. Phys.* **22**, 16053–16071 (2022).

25. J. Shutter, F. Keutsch, *Biosphere-Atmosphere Interactions* (American Chemical Society, 2021); https://doi.org/10.1021/acsinfocus.7e5007.

26. A. B. Guenther, X. Jiang, C. L. Heald, T. Sakulyanontvittaya, T. Duhl, L. K. Emmons, X. Wang, The model of emissions of gases and aerosols from nature version 2.1 (MEGAN2.1): An extended and updated framework for modeling biogenic emissions. *Geosci. Model Dev.* **5**, 1471–1492 (2012).

27. K. C. Wells, D. B. Millet, V. H. Payne, M. J. Deventer, K. H. Bates, J. A. de Gouw, M. Graus, C. Warneke, A. Wisthaler, J. D. Fuentes, Satellite isoprene retrievals constrain emissions and atmospheric oxidation. *Nature* **585**, 225–233 (2020).

28. D. Fu, D. B. Millet, K. C. Wells, V. H. Payne, S. Yu, A. Guenther, A. Eldering, Direct retrieval of isoprene from satellite-based infrared measurements. *Nat. Commun.* **10**, 3811 (2019).

29. R. M. Hoesly, S. J. Smith, L. Feng, Z. Klimont, G. Janssens-Maenhout, T. Pitkanen, J. J. Seibert, L. Vu, R. J. Andres, R. M. Bolt, T. C. Bond, L. Dawidowski, N. Kholod, J. Kurokawa, M. Li, L. Liu, Z. Lu, M. C. P. Moura, P. R. O'Rourke, Q. Zhang, Historical (1750–2014) anthropogenic emissions of reactive gases and aerosols from the Community Emissions Data System (CEDS). *Geosci. Model Dev.* **11**, 369–408 (2018).

30. P. O'Rourke, S. Smith, A. Mott, H. Ahsan, E. McDuffie, M. Crippa, Z. Klimont, B. McDonald, S. Wang, M. Nicholson, L. Feng, R. Hoesly, CEDS v_2021_04_21 Gridded emissions data, Pacific Northwest National Laboratory (2021); https://doi.org/10.25584/PNNLDATAHUB/1779095.

31. US EPA, National Tier 1 CAPS Trends (2022); https://epa.gov/air-emissions-inventories/air-pollutant-emissions-trends-data.

32. R. F. Silvern, D. J. Jacob, L. J. Mickley, M. P. Sulprizio, K. R. Travis, E. A. Marais, R. C. Cohen, J. L. Laughner, S. Choi, J. Joiner, L. N. Lamsal, Using satellite observations of tropospheric NO_2 columns to infer long-term trends in US NO_x emissions: The importance of accounting for the free tropospheric NO_2 background. *Atmos. Chem. Phys.* **19**, 8863–8878 (2019).

33. B. N. Duncan, L. N. Lamsal, A. M. Thompson, Y. Yoshida, Z. Lu, D. G. Streets, M. M. Hurwitz, K. E. Pickering, A space-based, high-resolution view of notable changes in urban NO_x pollution around the world (2005–2014). *J. Geophys. Res. Atmos.* **121**, 976–996 (2016).

34. J. Lelieveld, T. M. Butler, J. N. Crowley, T. J. Dillon, H. Fischer, L. Ganzeveld, H. Harder, M. G. Lawrence, M. Martinez, D. Taraborrelli, J. Williams, Atmospheric oxidation capacity sustained by a tropical forest. *Nature* **452**, 737–740 (2008).

35. J. L. Laughner, J. L. Neu, D. Schimel, P. O. Wennberg, K. Barsanti, K. W. Bowman, A. Chatterjee, B. E. Croes, H. L. Fitzmaurice, D. K. Henze, J. Kim, E. A. Kort, Z. Liu, K. Miyazaki, A. J. Turner, S. Anenberg, J. Avise, H. Cao, D. Crisp, J. A. de Gouw, A. Eldering, J. C. Fyfe, D. L. Goldberg, K. R. Gurney, S. Hasheminassab, C. E. Ivey, D. B. A. Jones, J. Liu, N. S. Lovenduski, R. V. Martin, G. A. McKinley, L. Ott, B. Poulter, M. Ru, S. P. Sander, N. Swart, Y. L. Yung, Z.-C. Zeng, Societal shifts due to COVID-19 reveal large-scale complexities and feedbacks between atmospheric chemistry and climate change. *Proc. Natl. Acad. Sci. U.S.A.* **118**, e2109481118 (2021).

36. H. Simon, A. Reff, B. Wells, J. Xing, N. Frank, Ozone trends across the United States over a period of decreasing NO_x and VOC emissions. *Environ. Sci. Technol.* **49**, 186–195 (2015).

37. C. L. Blanchard, G. M. Hidy, S. Shaw, K. Baumann, E. S. Edgerton, Effects of emission reductions on organic aerosol in the southeastern United States. *Atmos. Chem. Phys.* **16**, 215–238 (2016).

38. E. A. Marais, D. J. Jacob, J. L. Jimenez, P. Campuzano-Jost, D. A. Day, W. Hu, J. Krechmer, L. Zhu, P. S. Kim, C. C. Miller, J. A. Fisher, K. Travis, K. Yu, T. F. Hanisco, G. M. Wolfe, H. L. Arkinson, H. O. T. Pye, K. D. Froyd, J. Liao, V. F. McNeill, Aqueous-phase mechanism for secondary organic aerosol formation from isoprene: Application to the Southeast United States and co-benefit of SO_2 emission controls. *Atmos. Chem. Phys.* **16**, 1603–1618 (2016).

39. E. A. Marais, D. J. Jacob, J. R. Turner, L. J. Mickley, Evidence of 1991–2013 decrease of biogenic secondary organic aerosol in response to SO_2 emission controls. *Environ. Res. Lett.* **12**, 054018 (2017).

40. Y. Zheng, J. A. Thornton, N. L. Ng, H. Cao, D. K. Henze, E. E. McDuffie, W. Hu, J. L. Jimenez, E. A. Marais, E. Edgerton, J. Mao, Long-term observational constraints of organic aerosol dependence on inorganic species in the Southeast US. *Atmos. Chem. Phys.* **20**, 13091–13107 (2020).

41. A. J. Boris, S. Takahama, A. T. Weakley, B. M. Debus, S. L. Shaw, E. S. Edgerton, T. Joo, N. L. Ng, A. M. Dillner, Quantifying organic matter and functional groups in particulate matter filter samples from the southeastern United States – Part 2: Spatiotemporal trends. *Atmos. Meas. Tech.* **14**, 4355–4374 (2021).

42. J. Li, J. Mao, A. M. Fiore, R. C. Cohen, J. D. Crounse, A. P. Teng, P. O. Wennberg, B. H. Lee, F. D. Lopez-Hilfiker, J. A. Thornton, J. Peischl, I. B. Pollack, T. B. Ryerson, P. Veres, J. M. Roberts, J. A. Neuman, J. B. Nowak, G. M. Wolfe, T. F. Hanisco, A. Fried, H. B. Singh, J. Dibb, F. Paulot, L. W. Horowitz, Decadal changes in summertime reactive oxidized nitrogen and surface ozone over the Southeast United States. *Atmos. Chem. Phys.* **18**, 2341–2361 (2018).

43. D. B. Millet, M. Baasandorj, L. Hu, D. Mitroo, J. Turner, B. J. Williams, Nighttime chemistry and morning isoprene can drive urban ozone downwind of a major deciduous forest. *Environ. Sci. Technol.* **50**, 4335–4342 (2016).

44. C. Wiedinmyer, J. Greenberg, A. Guenther, B. Hopkins, K. Baker, C. Geron, P. I. Palmer, B. P. Long, J. R. Turner, G. Pétron, P. Harley, T. E. Pierce, B. Lamb, H. Westberg, W. Baugh, M. Koerber, M. Janssen, Ozarks Isoprene Experiment (OZIE): Measurements and modeling of the "isoprene volcano". *J. Geophys. Res.* **110**, D18307 (2005).

45. M. Hoerling, J. Eischeid, A. Kumar, R. Leung, A. Mariotti, K. Mo, S. Schubert, R. Seager, Causes and predictability of the 2012 Great Plains Drought. *Bull. Am. Meteorol. Soc.* **95**, 269–282 (2014).

46. M. D. Schwartz, T. R. Ault, J. L. Betancourt, Spring onset variations and trends in the continental United States: Past and regional assessment using temperature-based indices. *Int. J. Climatol.* **33**, 2917–2922 (2013).

47. US EPA, Climate Change Indicators in the United States, 3rd ed. (EPA 430-R-14-004, U.S. Environmental Protection Agency, Washington, D.C., 2014); www.epa.gov/climatechange/indicators.

48. T. R. Ault, G. M. Henebry, K. M. de Beurs, M. D. Schwartz, J. L. Betancourt, D. Moore, The false spring of 2012, earliest in North American record. *Eos Trans. Am. Geophys. Union* **94**, 181–182 (2013).

49. S. E. Pusede, A. L. Steiner, R. C. Cohen, Temperature and recent trends in the chemistry of continental surface ozone. *Chem. Rev.* **115**, 3898–3918 (2015).

50. R. Seco, T. Karl, A. Guenther, K. P. Hosman, S. G. Pallardy, L. Gu, C. Geron, P. Harley, S. Kim, Ecosystem-scale volatile organic compound fluxes during an extreme drought in a broadleaf temperate forest of the Missouri Ozarks (central USA). *Glob. Change Biol.* **21**, 3657–3674 (2015).

51. Comprehensive Statistics, U.S. Drought Monitor (April 11, 2023); https://droughtmonitor.unl.edu/DmData/DataDownload/ComprehensiveStatistics.aspx.

52. El Niño Index Dashboard: NOAA Physical Sciences Laboratory; https://psl.noaa.gov/enso/dashboard.html.

53. J. Liu, K. W. Bowman, D. S. Schimel, N. C. Parazoo, Z. Jiang, M. Lee, A. A. Bloom, D. Wunch, C. Frankenberg, Y. Sun, C. W. O'Dell, K. R. Gurney, D. Menemenlis, M. Gierach, D. Crisp, A. Eldering, Contrasting carbon cycle responses of the tropical continents to the 2015–2016 El Niño. *Science* **358**, eaam5690 (2017).

54. B. N. Duncan, I. Bey, M. Chin, L. J. Mickley, T. D. Fairlie, R. V. Martin, H. Matsueda, Indonesian wildfires of 1997: Impact on tropospheric chemistry. *J. Geophys. Res.* **108**, 4458 (2003).

55. M. J. Rowlinson, A. Rap, S. R. Arnold, R. J. Pope, M. P. Chipperfield, J. McNorton, P. Forster, H. Gordon, K. J. Pringle, W. Feng, B. J. Kerridge, B. L. Latter, R. Siddans, Impact of El Niño–Southern Oscillation on the interannual variability of methane and tropospheric ozone. *Atmos. Chem. Phys.* **19**, 8669–8686 (2019).

56. D. C. Anderson, B. N. Duncan, A. M. Fiore, C. B. Baublitz, M. B. Follette-Cook, J. M. Nicely, G. M. Wolfe, Spatial and temporal variability in the hydroxyl (OH) radical: Understanding the role of large-scale climate features and their influence on OH through its dynamical and photochemical drivers. *Atmos. Chem. Phys.* **21**, 6481–6508 (2021).

57. A. J. Turner, I. Fung, V. Naik, L. W. Horowitz, R. C. Cohen, Modulation of hydroxyl variability by ENSO in the absence of external forcing. *Proc. Natl. Acad. Sci. U.S.A.* **115**, 8931–8936 (2018).

58. Y. Zhao, M. Saunois, P. Bousquet, X. Lin, A. Berchet, M. I. Hegglin, J. G. Canadell, R. B. Jackson, M. Deushi, P. Jöckel, D. Kinnison, O. Kirner, S. Strode, S. Tilmes, E. J. Dlugokencky, B. Zheng, On the role of trend and variability in the hydroxyl radical (OH) in the global methane budget. *Atmos. Chem. Phys.* **20**, 13011–13022 (2020).

59. V. Huijnen, M. J. Wooster, J. W. Kaiser, D. L. A. Gaveau, J. Flemming, M. Parrington, A. Inness, D. Murdiyarso, B. Main, M. van Weele, Fire carbon emissions over maritime southeast Asia in 2015 largest since 1997. *Sci. Rep.* **6**, 26886 (2016).

60. R. D. Field, G. R. van der Werf, T. Fanin, E. J. Fetzer, R. Fuller, H. Jethva, R. Levy, N. J. Livesey, M. Luo, O. Torres, H. M. Worden, Indonesian fire activity and smoke pollution in 2015 show persistent nonlinear sensitivity to El Niño-induced drought. *Proc. Natl. Acad. Sci. U.S.A.* **113**, 9204–9209 (2016).

61. K. C. Wells, D. B. Millet, V. H. Payne, C. Vigouroux, C. A. B. Aquino, M. De Mazière, J. A. de Gouw, M. Graus, T. Kurosu, C. Warneke, A. Wisthaler, Next-generation isoprene measurements from space: Detecting daily variability at high resolution. *J. Geophys. Res. Atmos.* **127**, e2021JD036181 (2022).

62. C. R. Nowlan, G. González Abad, H.-A. Kwon, Z. Ayazpour, C. Chan Miller, K. Chance, H. Chong, X. Liu, E. O'Sullivan, H. Wang, L. Zhu, I. De Smedt, C. Seftor, K. Sun, Global formaldehyde products from the Ozone Mapping and Profiler Suite (OMPS) Nadir Mappers on Suomi NPP and NOAA-20. *Earth Space Sci.* **10**, e2022EA002643 (2023).

63. K. Sun, L. Zhu, K. Cady-Pereira, C. Chan Miller, K. Chance, L. Clarisse, P.-F. Coheur, G. González Abad, G. Huang, X. Liu, M. Van Damme, K. Yang, M. Zondlo, A physics-based approach to oversample multi-satellite, multispecies observations to a common grid. *Atmos. Meas. Tech.* **11**, 6679–6701 (2018).

64. H.-A. Kwon, G. González Abad, C. R. Nowlan, H. Chong, A. H. Souri, C. Vigouroux, A. Röhling, R. Kivi, M. Makarova, J. Notholt, M. Palm, H. Winkler, Y. Té, R. Sussmann,

M. Rettinger, E. Mahieu, K. Strong, E. Lutsch, S. Yamanouchi, T. Nagahama, J. W. Hannigan, M. Zhou, I. Murata, M. Grutter, W. Stremme, M. De Mazière, N. Jones, D. Smale, I. Morino, Validation of OMPS Suomi NPP and OMPS NOAA-20 formaldehyde total columns with NDACC FTIR observations. *Earth Space Sci.* **10**, e2022EA002778 (2023).

65. I. De Smedt, N. Theys, H. Yu, T. Danckaert, C. Lerot, S. Compernolle, M. Van Roozendael, A. Richter, A. Hilboll, E. Peters, M. Pedergnana, D. Loyola, S. Beirle, T. Wagner, H. Eskes, J. van Geffen, K. F. Boersma, P. Veefkind, Algorithm theoretical baseline for formaldehyde retrievals from S5P TROPOMI and from the QA4ECV project. *Atmos. Meas. Tech.* **11**, 2395–2426 (2018).

66. M. Friedl, D. Sulla-Menashe, MCD12Q1 MODIS/Terra+Aqua Land Cover Type Yearly L3 Global 500m SIN Grid V006, (2019); https://doi.org/10.5067/MODIS/MCD12Q1.006.

67. P. I. Palmer, D. J. Jacob, A. M. Fiore, R. V. Martin, K. Chance, T. P. Kurosu, Mapping isoprene emissions over North America using formaldehyde column observations from space. *J. Geophys. Res.* **108**, 4180 (2003).

68. D. B. Millet, D. J. Jacob, K. F. Boersma, T.-M. Fu, T. P. Kurosu, K. Chance, C. L. Heald, A. Guenther, Spatial distribution of isoprene emissions from North America derived from formaldehyde column measurements by the OMI satellite sensor. *J. Geophys. Res.* **113**, D02307 (2008).

69. K. H. Bates, D. J. Jacob, A new model mechanism for atmospheric oxidation of isoprene: Global effects on oxidants, nitrogen oxides, organic products, and secondary organic aerosol. *Atmos. Chem. Phys.* **19**, 9613–9640 (2019).

70. S. K. Akagi, R. J. Yokelson, C. Wiedinmyer, M. J. Alvarado, J. S. Reid, T. Karl, J. D. Crounse, P. O. Wennberg, Emission factors for open and domestic biomass burning for use in atmospheric models. *Atmos. Chem. Phys.* **11**, 4039–4072 (2011).

71. L. Giglio, J. T. Randerson, G. R. van der Werf, Analysis of daily, monthly, and annual burned area using the fourth-generation global fire emissions database (GFED4). *J. Geophys. Res. Biogeosci.* **118**, 317–328 (2013).

72. M. Mu, J. T. Randerson, G. R. van der Werf, L. Giglio, P. Kasibhatla, D. Morton, G. J. Collatz, R. S. DeFries, E. J. Hyer, E. M. Prins, D. W. T. Griffith, D. Wunch, G. C. Toon, V. Sherlock, P. O. Wennberg, Daily and 3-hourly variability in global fire emissions and consequences for atmospheric model predictions of carbon monoxide. *J. Geophys. Res.* **116**, D24303 (2011).

73. J. T. Randerson, Y. Chen, G. R. van der Werf, B. M. Rogers, D. C. Morton, Global burned area and biomass burning emissions from small fires. *J. Geophys. Res.* **117**, G04012 (2012).

74. G. R. van der Werf, J. T. Randerson, L. Giglio, T. T. van Leeuwen, Y. Chen, B. M. Rogers, M. Mu, M. J. E. van Marle, D. C. Morton, G. J. Collatz, R. J. Yokelson, P. S. Kasibhatla, Global fire emissions estimates during 1997–2016. *Earth Syst. Sci. Data* **9**, 697–720 (2017).

75. R. C. Hudman, N. E. Moore, A. K. Mebust, R. V. Martin, A. R. Russell, L. C. Valin, R. C. Cohen, Steps towards a mechanistic model of global soil nitric oxide emissions: Implementation and space based-constraints. *Atmos. Chem. Phys.* **12**, 7779–7795 (2012).

76. H. Weng, J. Lin, R. Martin, D. B. Millet, L. Jaeglé, D. Ridley, C. Keller, C. Li, M. Du, J. Meng, Global high-resolution emissions of soil NO_x, sea salt aerosols, and biogenic volatile organic compounds. *Sci. Data* **7**, 148 (2020).

77. L. T. Murray, D. J. Jacob, J. A. Logan, R. C. Hudman, W. J. Koshak, Optimized regional and interannual variability of lightning in a global chemical transport model constrained by LIS/OTD satellite data. *J. Geophys. Res.* **117**, D20307 (2012).

78. G. González Abad (2022), OMPS-NPP L2 NM Formaldehyde (HCHO) Total Column swath orbital V1, Greenbelt, MD, USA, Goddard Earth Sciences Data and Information Services Center (GES DISC), Accessed: 30 March 2023, https://doi.org/10.5067/IIM1GHT07QA8.

79. I. De Smedt, H. Yu, A. Richter, S. Beirle, H. Eskes, K. F. Boersma, M. Van Roozendael, J. Van Geffen, A. Lorente, E. Peters, QA4ECV HCHO tropospheric column data from OMI, Version 1.1, Royal Belgian Institute for Space Aeronomy (2017); https://doi.org/10.18758/71021031.